Micromechanical study of raw earth stabilization using instrumented indentation

Ugo De Filippis, Elodie Prud'Homme, Sylvain Meille

Micromechanical study of Raw Earth stabilization using instrumented indentation

Ugo De Filippis[a], Elodie Prud'homme[a], Sylvain Meille[a,*]

[a] Univ Lyon, INSA Lyon, UCBL, CNRS, MATEIS, UMR5510, 69621 Villeurbanne, France
*Corresponding author: sylvain.meille@insa-lyon.fr

Alkali-activated slag is used as a stabilizer in earthen materials to improve their mechanical properties and to reduce their sensitivity to water. The efficiency of this stabilization is assessed through the mechanical characterization of samples made of three stabilized raw earths (RE) with different mineralogical compositions and equilibrated under five different hygrometric conditions. Instrumented indentation tests are used to evaluate the cohesion of the stabilized samples as this testing method allows the characterization of the mechanical properties of brittle porous materials at a local scale. The results show an increase in hardness and elastic modulus and a strong decrease in water sensitivity of the three different RE with increasing slag and activator contents.

Keywords: Spherical indentation, Hardness, Raw Earth, water sensitivity, sustainable binder

1 Introduction

Earth-based materials have a great potential for reducing the environmental footprint of buildings due to their low environmental impact and their moisture and thermal buffering capacity [1−4]. However, the mechanical properties of raw earth (RE) materials and their sensitivity to water [5,6] are a strong limitation for a more widespread use. Currently, RE are stabilized with an addition of cement to improve compressive strength in dry and humid environments [7−10]. However, the addition of cement increases the environmental footprint of the material, significantly reduces its hygrothermal properties and thus its thermal and hydric buffering capacity [11−14]. A potential solution to limit these drawbacks is the stabilization of RE with alkali-activated slag, which has a lower global warming impact than cement [15−17]. However, only a few works have focused on the study of the mechanical properties of such materials and especially on the influence of relative humidity [18−22].

Regarding the mechanical properties of RE materials, the most common tests are the unconfined compressive strength (UCS) [20,22−24] and the triaxial shear stress test [20,25] on centimeter-sized samples. Yet a characterization of the mechanical properties at a local scale is needed to study the interactions between hydrates and clayey particles of the RE in stabilized samples. Instrumented indentation testing is a more suitable method for this purpose, enabling the determination of hardness H and elastic modulus E on small size samples [26−28]. These mechanical parameters are related to the cohesive forces that develop within the material, especially for granular cohesive-frictional materials such as RE [29−31]. Surface penetration testing is notably used in geotechnics to measure the mechanical resistance of soils. The interest in using a spherical indenter lies in the fact that it allows the characterization of heterogeneous samples and limits macro-cracking [32], a critical issue when testing brittle materials. Moreover, the measurements can be performed on small specimens, which is particularly critical when studying the fine granulometric fraction of RE as it reduces the consumption of raw material and limits shrinkage-induced cracking during curing. Finally, the test duration can be short, limiting the drying effects during measurements, and several tests can be performed on the same sample, facilitating data collection and further statistical analysis.

The main objective of this study is to characterize the mechanical efficiency of RE stabilization with slag using instrumented indentation. Only the fine granulometric fraction of the RE (< 400 µm) is considered in order to focus the study on the mechanical interactions between the clayey particles and the hydrates formed during slag hydration. In particular, the mechanical characterization is carried out over a large range of hygrometric conditions in order to study the water sensitivity of the samples, a critical parameter regarding earthen materials [23,25,33−35]. The use of local tests on specimens made only of the binding phase (slag and RE), this for different environmental conditions, represents an original approach as compared to previously published works.
The mechanical characterization is supported by microstructural investigations to study the influence of the stabilization on clayey particles, as described in a companion paper [36].

2 Material and Methods

2.1 Materials

Three different RE were studied to evaluate the impact of their mineralogy on the stabilization by alkali-activated slag. The RE labeled as FAC are residues of quarry washing sludge. Levens (Lev) and St-Martin (SM) are two natural REs from the south of France and provided by Filiater (Nice, France). The studied RE fractions are characterized by standardized geotechnical methods to assess their physicochemical properties (**Table 1**, see [36] for a detailed description of the experimental methods).

Table 1: Geotechnical characterization results of the three raw earths.

	FAC	**Levens (Lev)**	**St-Martin (SM)**
d_{10} / d_{50} / d_{90} (µm)	14 / 54 / 92	42 / 57 / 77	2 / 39 / 73
Dry density (g/cm^3)	2.54	2.47	2.63
Specific Surface Area (m^2/g)	25.5	44.1	58.0
Clay content	Slightly clayey	Moderately clayey	Moderately clayey
Mineral nature	**Calcite**, quartz, dolomite, kaolinite, muscovite	**Quartz, calcite,** muscovite, albite, kaolinite	**Quartz, calcite,** muscovite, albite, kaolinite

FAC mainly contains carbonated species such as calcite and dolomite, the clayey particles are kaolinite and muscovite. In particular, kaolinite has no significant surface charges and no specific interactions with water [37,38]. Lev and SM have similar compositions, their main components being quartz and calcite. Montmorillonite belongs to the smectite group and presents a high specific surface area, a high surface charge density and a high swelling potential due to water absorption [38–40]. Its presence in Lev and SM mainly explains their higher clayey activity as compared to FAC [41]. SM presents a slightly lower content of montmorillonite but a significantly higher content of muscovite than Lev, explaining its higher specific surface area.

The ground blast furnace slag (GBFS) used is provided by ECOCEM, France. Its physicochemical properties have been presented in a previous paper [42]. The alkaline solutions used for slag activation are two sodium hydroxide (NaOH) solutions of 4 and 12 M based on a previous work [42]. The 4 M solution is considered to be just above the minimal concentration required to achieve satisfactory activation of the slag after 28 days of curing. Conversely, the 12 M solution is just above the optimal concentration and corresponds to a slight excess of sodium concentration [42].

2.2 Samples Preparation

The samples are obtained by mixing together two primary pastes: the first one is made of RE mixed with deionized water and the second one is made of the alkali-activated slag paste in the fresh state. The latter is obtained by manually mixing anhydrous slag with the activating solution for 2 minutes. The slag paste is mixed with the wet RE paste immediately after its preparation to avoid any hardening. Thanks to the

deflocculation of slag grains in the activating solution, this protocol enables to obtain a homogenous mix and then a homogeneous distribution of the slag-based binder in the sample. The water to slag ratio and the water to RE ratio are kept constant and both equal to 0.4. The added slag content is evaluated through the ratio of the dry mass of slag to the dry mass of RE and is set to 0, 5, 8, 10, 12 or 15%. Samples with no added slag are formulated to have a similar sodium content as the formulations with 15% of added slag to study the effect of the addition of sodium hydroxide on the RE behavior. The samples without added slag are referred to as unstabilized samples.

After mixing, the samples are poured into prismatic molds with a cross-section of 4 x 6 mm^2 and a length of 40 mm. The molds are then kept in a controlled atmosphere of 23 ± 2°C and relative humidity (RH) greater than 95% to prevent drying shrinkage or moisture gradient in the sample. The samples are demolded after 24 hours and sealed in tightly closed plastic film and plastic bags to maintain endogenous conditions for curing. Mechanical tests and microstructural characterization are all performed after 28 days of curing.

The evolution of mechanical properties as a function of moisture content is studied on four specific formulations for each RE (**Table 2**) by conditioning the samples in five different hygrometric atmospheres using saturated hygroscopic salt solutions (**Table 3**). After 28 days of curing under endogenous conditions, the samples are unsealed and transferred to sealed boxes at different humidity levels and constant temperature (23 ± 1°C) until a constant mass is reached. The mass is considered constant when the difference between two consecutive measurements over 24 hours is less than 0.1%.

Table 2: List of the formulations studied in different hygrometric conditions and the associated sodium concentrations (in the activating solution, ratio of Na_2O/RE and total concentration in the sample) after mixing. RE* (raw earth) stands for: FAC (clay-limestone residues), Lev (Levens) or SM (St-Martin). The water to slag and water to RE mass ratio are both equal to 0.4.

Nomenclature	Slag / RE* (wt%)	$[Na]_{solution}$ (M)	Na_2O / RE* (wt%)	$[Na]_{sample}$ (M)
RE*_0_12M	0	12	2.25	1.81
RE*_5_12M	5	12	0.75	0.58
RE*_15_4M	15	4	0.75	0.53
RE*_15_12M	15	12	2.25	1.58

Table 3: Humidity levels and associated saturated salt solutions used for the RH controlled boxes at 23°C.

Relative Humidity (RH)	Saturated solution	Chemical formula
33 ±1%	Magnesium chloride	$MgCl_2$
45 ±3%	Potassium carbonate	K_2CO_3
65 ±3%	Ammonium nitrate	NH_4NO_3
85 ±2%	Potassium chloride	KCl
> 98 ±1%	Water	H_2O

2.3 *Characterization Methods*

Instrumented indentation

Instrumented indentation allows to measure the hardness and elastic modulus at a local scale [26], by monitoring the applied force and the penetration of the indenter into the material. In standard indentation tests, hardness *H* is typically measured by the ratio of the maximum applied load, P_{max} to the area of the hardness impression, *A*, left by the indenter on the surface of the material after complete unloading. In instrumented indentation, the determination of the contact area is made from the continuous measurement of the penetration depth during a loading-unloading cycle.

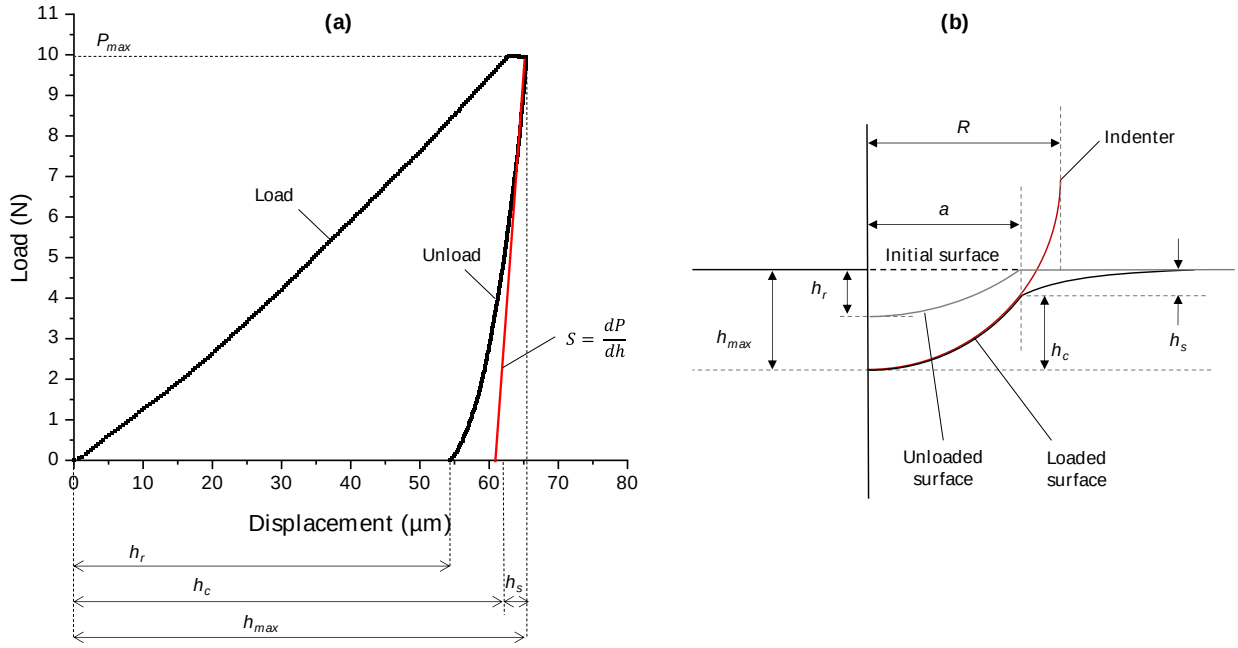

Fig. 1: (a) Typical load − displacement curve of an instrumented indentation test (black) and representation of the slope of the unload curve at the point of maximum force (red), a dwell at maximum load is applied to limit viscous effects during unloading. (b) Cross-sectional schematic representation of the test. h_r: residual depth, h_c: contact depth, h_{max}: maximum depth and h_s: elastic spring back.

Hardness *H*, is defined as the ratio between the maximum applied load, P_{max} and the projected area of contact between the indenter and the material, A_C:

$$H = \frac{P_{max}}{A_c} \tag{1}$$

It corresponds to the average contact pressure on the surface.

In the case of axisymmetric indenters, the Young's modulus can be determined using the following equation derived by Sneddon:

$$E_r = \frac{\sqrt{\pi}}{2}\frac{S}{\sqrt{A_c}} \tag{2}$$

with A_C the area of contact and S the slope of the unloading curve at the point of maximum load ($S = dP/dh$, **Fig. 1**.a), and E_r the reduced modulus defined as:

$$\frac{1}{E_r} = \frac{(1-\nu^2)}{E} + \frac{(1-\nu_i^2)}{E_i} \quad (3)$$

where E and E_i are the elastic modulus and ν and ν_i the Poisson's ratio of the material and of the indenter respectively.

The contact area between the indenter and the surface of the material depends on the penetration contact depth h_c (**Fig. 1**.b) and on the tip geometry. In the case of a perfect spherical indenter, they are related by the following relation:

$$A_c = \pi a^2 = 2\pi R h_c - \pi {h_c}^2 \quad (4)$$

with a the radius of the projected contact area and R the radius of the indenter (**Fig. 1**.b). The contact depth is determined from the total penetration depth using the following equation, as given by Oliver and Pharr [27]:

$$h_c = h_{max} - \epsilon \frac{P_{max}}{S} \quad (5)$$

with h_{max} the maximum penetration of the tip to the samples surface, P_{max} the maximum load, S the initial slope of the unloading curve and ϵ a geometrical parameter equal to 0.75 for a spherical indenter [27].

Therefore, hardness and elastic modulus depend on the determination of the slope of the unloading curve at maximum load (S). This slope can be calculated by two methods, either by a linear fit of the upper part of the unloading curve at the maximum load, or by the power law fit of the unloading curve through the following relationship [27] and the calculation of its derivative at maximum load:

$$P = C_e(h - h_f)^m$$

where C_e, m and h_f are the parameters of the fit.

Both methods are used in this work considering that the unloading curve fitting with a power law could be delicate due to some events in the curve and to the quality of the data set. The determination of the unloading slope is carried out using a home-made Matlab program [43] which also takes into account the stiffness corrections of the testing equipment. The use of Oliver and Pharr method has already been validated on spherical indentation tests on porous inorganic materials [26,32,44,45]. It has also been validated on the materials of interest in this work by measuring the contact radius of the residual imprint and by comparing it to the calculated value (**Fig. 2**). The difference between the experimentally observed contact radius and the calculated one is less than 2%. Furthermore, no piling up was observed around the residual impressions, as already noted for porous mineral materials prone to microcracking and densification under the impression [26,32,46].

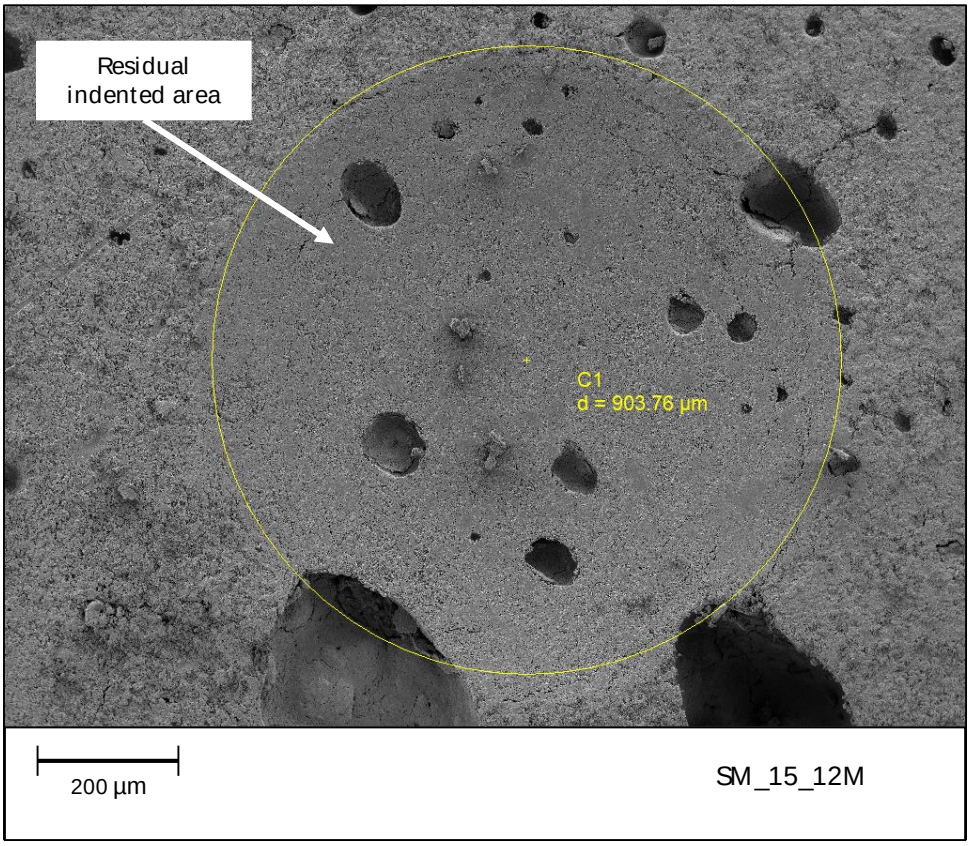

Fig. 2: SEM image (SE mode) of a residual impression on the SM_15_12M sample. P_{max} = 10 N, R = 1.5 mm, calculated contact radius from Eq. (4) and (5): a = 460 µm, measured contact radius (yellow circle) = 452 µm.

The tests are performed on an ElectroForce 3200 machine (TA instruments, USA) equipped with a 22 N load cell with a resolution of 0.05 N and a capacitive displacement transducer with a measurement range of ± 0.5 mm and a resolution of 0.5 µm. The load rate is kept constant to 0.32 N/s during loading. The maximum load is maintained during 5 s at the end of the loading cycle before unloading. The sample is mechanically held during the test to prevent macroscopic movements that could affect the displacement measurement.

The indenter used is a 3 mm diameter tungsten carbide sphere. The use of a relatively large sphere enables to test a sufficiently large volume of material to average the mechanical contributions of the different components such as the RE particles, the anhydrous and the hydrated slag and the pores. A similar approach has already been conducted on several brittle porous materials [26,32,44,46].

The maximum applied force is adjusted according to the characteristics of the material. On the one hand, it is limited in order to avoid a too large damaged zone, which would affect the determination of the elastic modulus of the material, and on the other hand, it must be sufficient to avoid the influence of the surface roughness of the sample, as already described in [26]. The surface roughness of the tested samples was measured with a RH-2000 high resolution optical microscope equipped with a non-contact confocal white light profilometer NPS (Nano point scanner) and a NP1 sensor (Hirox, Japan). The measured average surface roughness (Ra) of the samples ranges between 1 and 5 µm. The samples are not polished to avoid any degradation of the surface and because impregnation with a resin would change the properties of the samples. Therefore a minimum indentation depth of at least 40 µm, corresponding to a contact radius of 350 µm, was chosen in this work, to ensure that the test measures the average properties of the material,

as a minimum penetration depth of five times the surface roughness is considered as sufficient to limit the influence of roughness [32,47]. The corresponding applied load varies from 2 to 12 N depending on the formulation. The level of applied force used in this work is large enough to limit a possible indentation size effect noted for ceramics (typically below few mN [48]).
Typical load-displacement curves are shown in **Fig. 3**. A total of four tests are performed on each sample, with two different samples for each formulation, i.e. 8 tests per formulation. The centers of two consecutive indentations are distant by at least four times the contact radius to avoid interaction between two adjacent measurements [26,32].

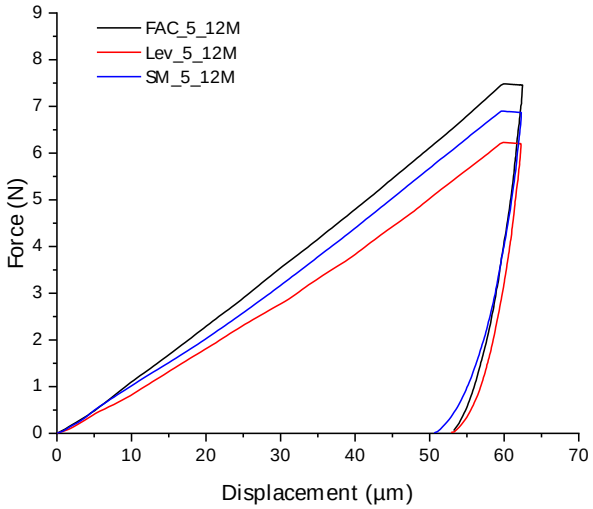

Fig. 3: Load - Displacement curve of samples stabilized with 5 wt% of slag and an activating solution of 12 M.

The correlation between the measured hardness and the measured elastic modulus is shown in **Fig. 4**. Despite some scatter in the experimental data, a clear correlation between the two parameters can be noted, as already found in literature on both porous ceramics [32,44] and bone tissue [49].

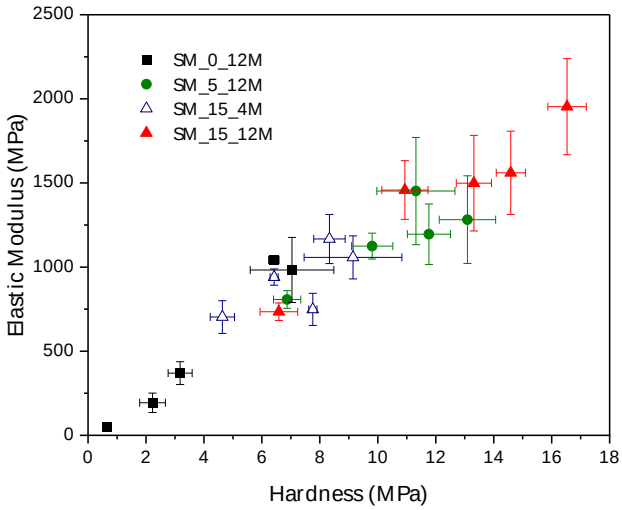

Fig. 4: Correlation between measured hardness and elastic modulus on all SM raw earth samples tested.

Therefore, in the following section only hardness values will be presented for the sake of comparison between the different formulations tested, especially since hardness values are slightly less scattered than elastic modulus values. However, it should be noted that, in the case of spherical indentation, the hardness values are not intrinsic to a material but increase with the depth of penetration in the material [50] (**Fig. 5**). In fact, for small applied loads the behavior can be considered as mainly elastic, possibly described by the Hertz theory of elastic contact. As the applied load increases, a damaged zone is progressively created under the indenter, with an increase in the residual penetration depth. Hardness versus the ratio of contact radius to the sphere radius, *a/R*, is often plotted to characterize a material behavior in instrumented indentation and is referred to as a "contact stress-strain" curve (**Fig. 5**) [50]. Note that other definitions of indentation strain exist in literature [51,52].

In this study, all the results presented are obtained with a 3 mm diameter sphere and at a similar penetration depth, and therefore at a similar range of *a/R* ratio (**Fig. 1**.b), ranging between 0.45 and 0.60 depending on the formulations. For inorganic porous materials, the increase in hardness with penetration depth is very pronounced after the creation of a damaged zone below the surface and an almost constant hardness value is obtained for a sufficient penetration depth [32], which is the case in this work for *a/R* values above 0.45 (**Fig. 5**).

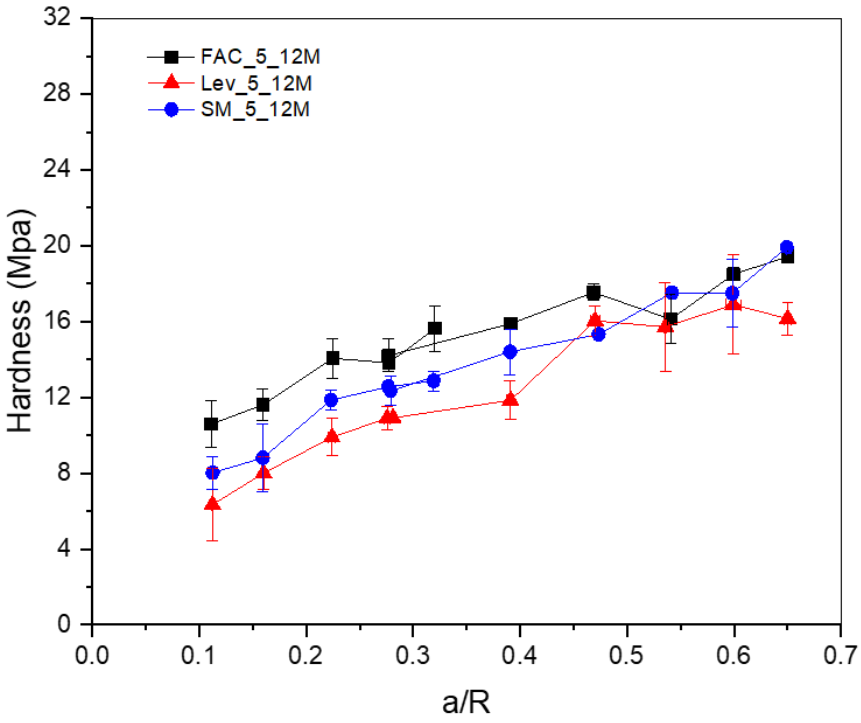

Fig. 5: Evolution of hardness with the depth of indentation expressed as the *a/R* ratio (contact radius on sphere radius) for samples stabilized with 5 wt% of slag and an activating solution of 12 M.

Characterization of hydric properties

The water content *W* of the samples was measured immediately after the indentation test. The wet mass of the samples m_{wet}, after conditioning in different environmental conditions, is measured before placing the sample in an oven at 105 °C until constant mass. The dry mass of the samples m_d is then measured and the water content is calculated from the relation:

$$W = \frac{m_{wet} - m_d}{m_d} \tag{6}$$

The total capillary pore volume *V* was obtained considering that near saturation in humidity (RH = 98%) all the pore volume in which capillary condensation may appear is filled by liquid water. Thus, the capillary pore volume is given by:

$$V = m_{w,98\%}/\rho_w \tag{7}$$

with $m_{w,98\%}$ the mass of water in the sample at 98% RH ($m_{w,98\%} = W(98\%) \cdot m_d$) and ρ_w the density of water at 23°C (ρ_w = 0.997 g/cm^3).

The molar quantity of adsorbed water (n^a, mmol/g) was determined as follows:

$$n^a = \frac{m_w}{M_{H_2O}} \times 10^3 = \frac{W \cdot m_d}{M_{H_2O}} \times 10^3 \quad (8)$$

The water content of the samples conditioned at different RH levels (**Table 3**) is used to determine the specific surface area of the samples by applying the BET method [53,54]. The BET equation gives the relationship between the adsorbed water and the relative pressure of water [55]:

$$n^a = n_m^a \cdot \frac{Cx}{(1-x)(1-x+Cx)} \quad (9)$$

where n^a is the molar quantity of adsorbed water, n_m^a is the molar quantity of water needed to cover the accessible surface with a monolayer of molecules, C is the BET constant of the material and x is the relative pressure of water ($x = \frac{P}{P_0} = \mathrm{RH}(\%)/100$).

The experimental quantity of adsorbed water versus the relative pressure of water *x* was interpolated using the Akima split method on OriginPro software to obtain a continuous curve of adsorption from the discrete experimental data points. To determine the parameters C and n_m^a, the interpolated data are fitted with the linearized expression of the BET equation (Eq. (10)) in the linear range of adsorption, which was here considered between 0.1 < *x* < 0.3.

$$\frac{x}{n^a(1-x)} = \frac{1}{n_m^a C} + \left[\frac{C-1}{n_m^a C}\right] x = b + sx \quad (10)$$

with s and b the slope and intercept respectively of the linear fit which enable to determine C and n_m^a through the following relations:

$$C = \frac{s}{b} + 1 \quad (11)$$

$$n_m^a = \frac{1}{b \cdot C} \quad (12)$$

The specific surface area *A* was then obtained with the following equation:

$$A = n_m^a \cdot N \cdot a_m \quad (13)$$

with N the Avogadro number and a_m the molecular cross-sectional area of water (a_m = 1.15 x 10^{-19} m² [56]).

Characterization of microstructure

Scanning electron microscopy (SEM) observations were performed on a Vega 3 SEM (Tescan, Czech Republic). Observations were made on gold coated samples using back scattering electron (BSE) mode, with an acceleration voltage of 5 kV and a working distance of 5 mm.

3 Results

3.1 Indentation Results for Endogenous-cured Samples

Hardness measurements on the samples cured under endogenous conditions for 28 days are shown in **Fig. 6** as a function of the added slag content and for the two concentrations of the activating solution (4 and 12 M). For FAC and Lev samples, the evolution of hardness with increasing slag content is similar and presents three main phases: an increase between 5 wt% and 8 wt%, followed by a plateau up to 12 wt% and by a significant increase at 15 wt%. This evolution can be explained by an increase in the volume fraction of hydrated slag (see section 3.4). Nevertheless, some differences can be noted depending on the nature of the RE. Especially, no significant evolution in hardness is noted for FAC samples between the 4 and 12 M activating solution (**Fig. 6**.a) on contrary to what is observed on Lev samples stabilized when the slag content is above 5 wt% (**Fig. 6**.b). Moreover, a significant increase in hardness is observed for Lev from 12 wt% of slag with 12 M activating solution whereas it is observed from 15 wt% for the FAC samples and the Lev samples stabilized with the 4 M solution. It is worth noting that, under endogenous conditions, the hardness values obtained with Lev are the highest among all the samples tested.

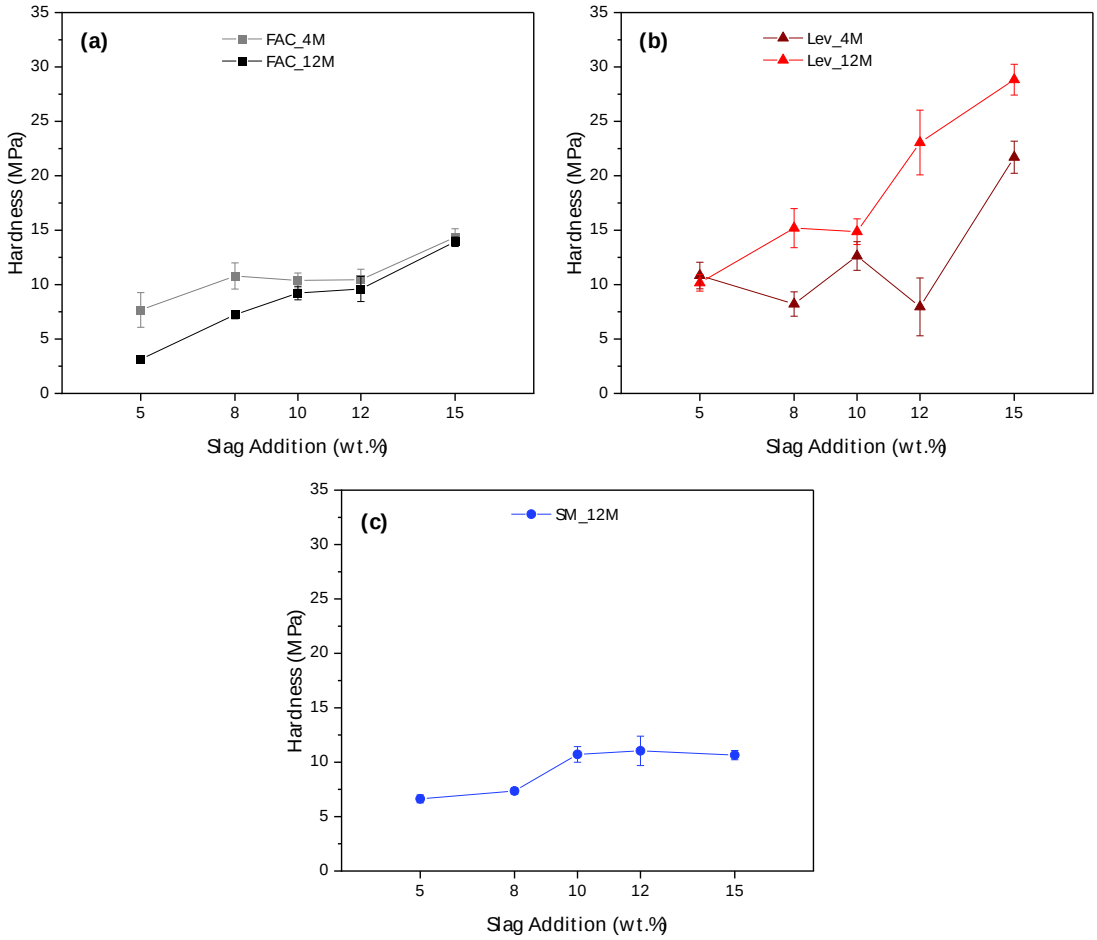

Fig. 6: Evolution of hardness at 28 days for samples cured in endogenous conditions as a function of the content of added slag and the sodium concentration of the activating solution for (a) FAC, (b) Lev and (c) SM raw earths.

For SM samples (**Fig. 6**.c), only the results for the 12 M activating solution are presented. Indeed, the addition of sodium hydroxide to a raw earth modifies its rheological behavior through the flocculation or deflocculation of clayey particles due to the interaction with Na^+ cations of the activating solution [57–59]. In the case of the SM raw earth, which presents the highest clayey content (**Table 1**), this flocculating effect is too important to allow a satisfactory preparation of the samples with the 4 M activating solution on the whole range of slag addition studied and in particular for slag contents lower than 10 wt%. In these conditions, the stabilized paste obtained after mixing is not fluid enough to cast proper samples for indentation measurements. However, when the 12 M solution is used, the sodium content is sufficiently high to achieve a deflocculating effect and samples can be cast. SM samples stabilized with the 12 M activating solution present a different evolution of hardness with increasing slag content as compared to the other two RE. First a slight increase up to 10 wt% of added slag is noted, followed by a plateau value above 10% of slag content.

3.2 Indentation Results with RH Level

The influence of water absorption on hardness of the samples conditioned under controlled humidity is first presented for samples containing sodium hydroxide but without slag addition, by plotting the hardness versus the relative humidity (**Fig. 7**.a) or the water content (**Fig. 7**.b).

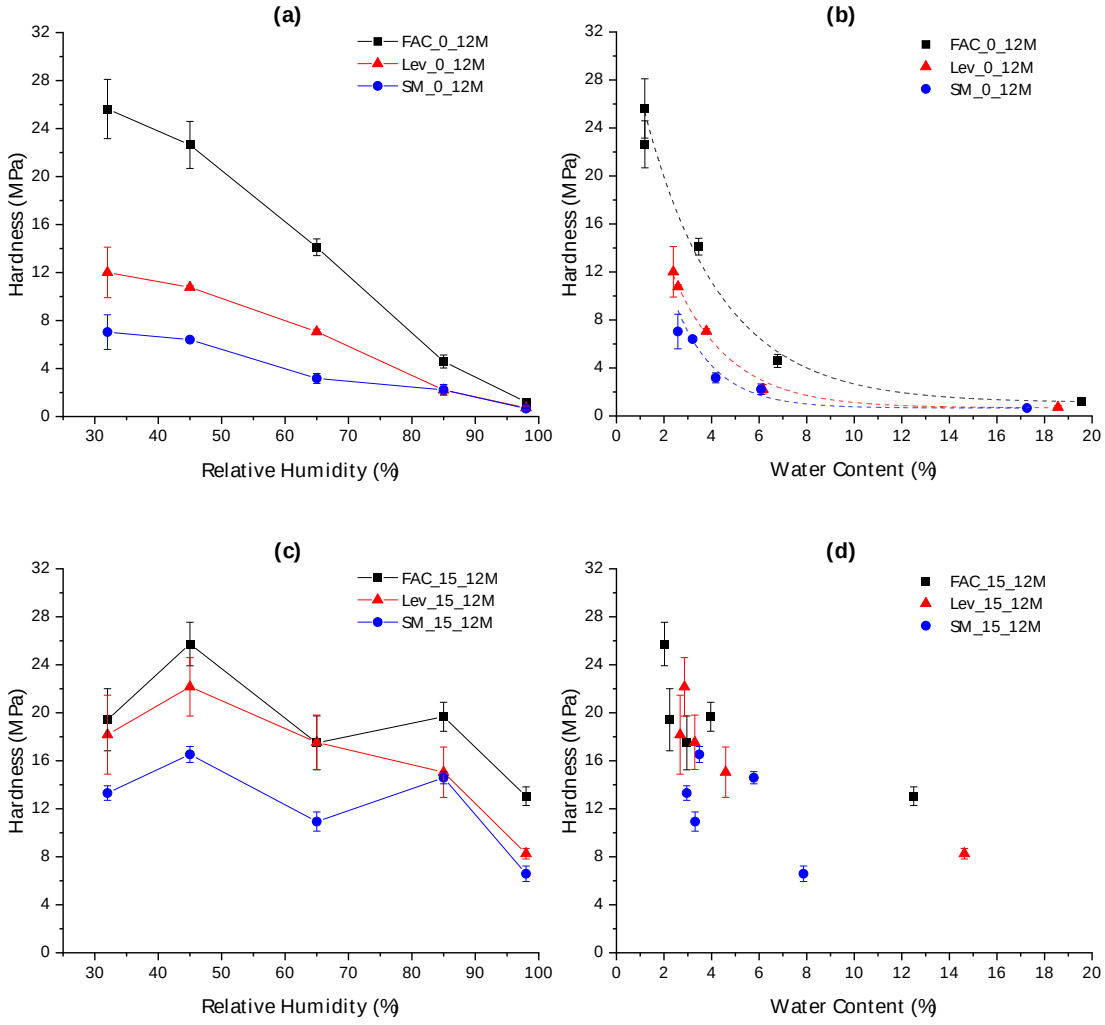

Fig. 7: Evolution of hardness versus (a, c) relative humidity and (b, d) water content for the samples with sodium hydroxide addition only (a, b) and for samples with 15 wt% of slag addition (c, d). The dashed lines represented in (b) correspond to exponential fits (**Table 4**).

All the unstabilized samples show a significant decrease in hardness with increasing RH (**Fig. 7**.a) or water content (**Fig. 7**.b). The decrease is significant for RH values higher than 45%, corresponding to water contents higher than 3.3%. The minimal hardness, almost equal to zero, is reached when the RH is equal to 98% (FAC: 1.2 MPa – Lev and SM: 0.7 MPa), corresponding to a maximal water content in the samples (> 15%). The decrease in hardness with the water content follows an exponential decay for the three RE. The equations and correlation coefficients are given in **Table 4**.

Table 4: Literal expression, numerical parameters and correlation coefficients (R^2) of the exponential fit of hardness (*H*) evolution with water content (*W*) (**Fig. 7**.b).

Equation	$H = a + b \cdot exp(-c \cdot W)$			
	a	*b*	*c*	R^2
FAC_0_12M	1.12 ± 0.18	35.11 ± 4.95	0.31 ± 0.04	0.989
Lev_0_12M	0.68 ± 0.23	30.21 ± 3.76	0.42 ± 0.05	0.998
SM_0_12M	0.66 ± 0.05	37.21 ± 19.77	0.59 ± 0.16	0.994

For low (< 45% RH) and medium (< 65% RH) relative humidities, the measured hardness is significantly different for the three RE. Unlike the samples kept under endogenous conditions (**Fig. 6**), hardness values for the FAC samples are higher and the decrease with RH or water content is more pronounced than for SM and Lev, as evidenced by the lower exponential constant (*c*) for this sample (**Table 4**). Lev presents intermediate hardness values and SM the lowest.

Evolution of hardness with either the RH or the water content is also shown for stabilized samples with 15 wt% of slag addition and a 12 M sodium hydroxide solution (**Fig. 7**.c-d). On the one hand, the difference in hardness between the three RE is significantly reduced as compared to unstabilized samples (**Fig. 7**.a). In particular, at relative humidities lower than 45%, the stabilized samples present an important increase in hardness for both Lev (+77% at RH = 45%) and SM (+122% at RH = 45%) as compared to unstabilized samples, while the hardness for FAC is almost constant (-6%, for RH = 45%). Hence, the hardening due to the addition of slag depends on the mineralogy of the raw earth and is higher for Lev and SM than for the FAC.

On the other hand, the water sensitivity of hardness is strongly reduced with slag addition, with no significant decrease noted up to 85% RH. Besides, the values obtained at 98% RH are significantly higher than those of the unstabilized samples: 13.1 MPa, 8.3 MPa and 6.6 MPa for the FAC, Lev and SM samples respectively. The loss in hardness at 98% RH as compared to 33% RH, is significantly reduced for stabilized FAC samples (−33%) and, to a lesser extent, for Lev (-55%) and SM (-51%) samples. The maximum water content is also reduced for stabilized samples as compared to unstabilized ones. This reduction is greater for SM (-54%) than for Lev (-21%) and the FAC (-36%). Finally, even though hardness decreases globally with water content (**Fig. 7**.d), no satisfactory correlation between hardness and water content can be found for stabilized samples. The water content above which the decrease in hardness becomes significant is above 6%, twice the value observed for unstabilized samples (**Fig. 7**.b).

The influence of formulation on the efficiency of slag stabilization is studied through the evolution of hardness and water content with the RH level for all the formulations of the three RE tested (**Fig. 8**).

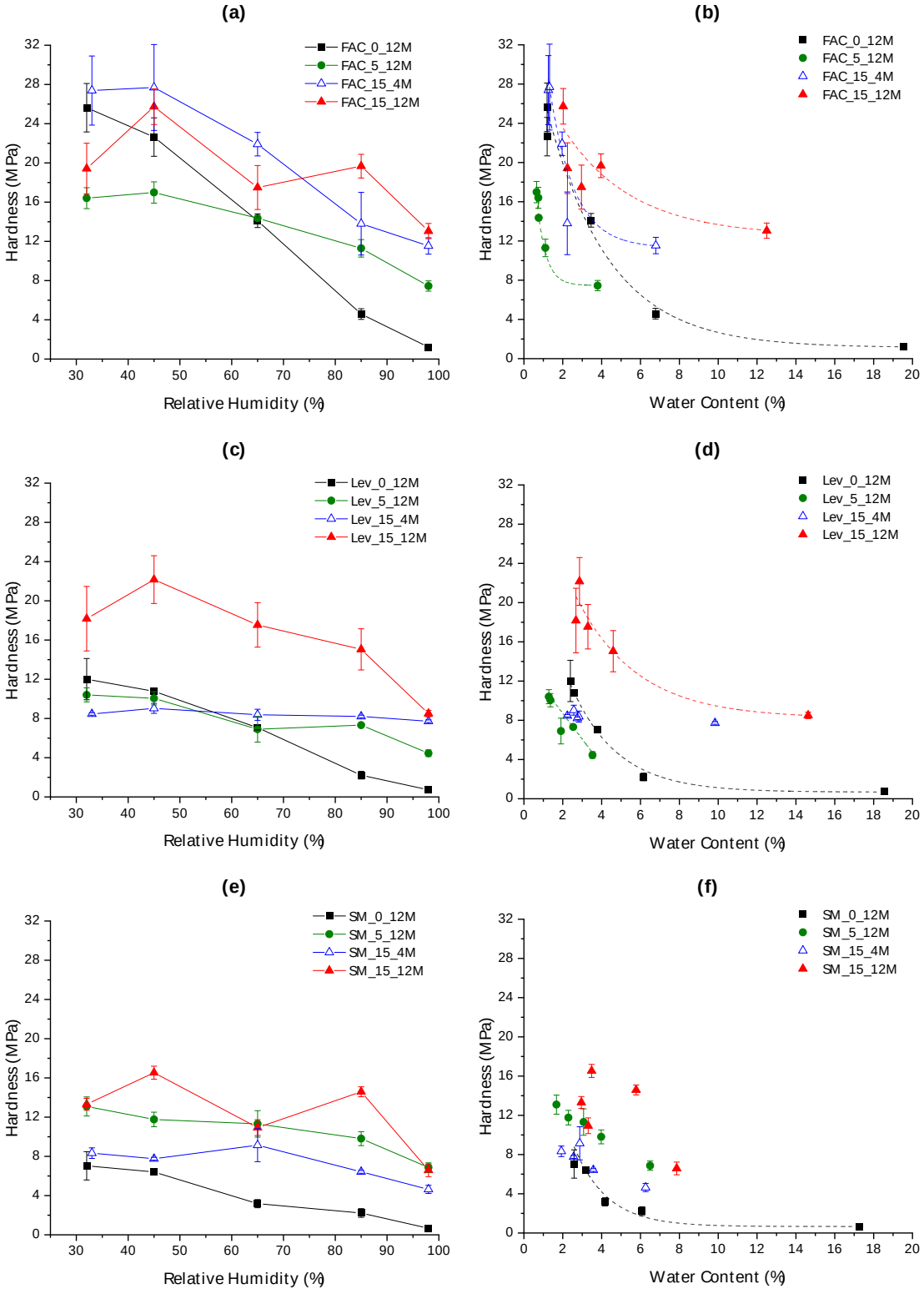

Fig. 8: Evolution of hardness as a function of (a, c, e) the conditioning relative humidity and of (b, d, f) the water content measured on (a, b) FAC, (c, d) Lev and (e, f) SM samples. The dashed lines in b, d, f are guides to the eye.

Regarding the hardness evolution with RH (**Fig. 8**.a, c, e), two main ranges of RH can be identified, below and above 65% RH:

- In the low RH range, the hardness increases due to stabilization and strongly depends on the nature of the RE.
- Conversely, in the high RH range, all the stabilized formulations present higher hardness values as compared to the samples with no slag addition (labelled RE*_0_12M), although the extent of the improvement also depends on the nature of the RE. For RE*_15_12M, FAC samples present the highest hardness (13.1 MPa) before Lev (8.5 MPa) and then SM (6.6 MPa) samples. In addition, all the stabilized samples show a reduced water content at high RH but this reduction also depends on the nature of the RE (**Fig. 8**.b, d, f).

Regarding more specifically the FAC samples, there are no significant differences in the hardness evolution with humidity between the two samples stabilized with 15 wt% of slag, i.e. activated with 4 M and 12 M solutions (**Fig. 8**.a). Both present higher hardness values than the sample with only 5 wt% of slag. Nonetheless, the water content at high humidity of the FAC_15_4M sample is much lower than the FAC_15_12M (**Fig. 8**.b) and the FAC_15_12M formulation shows higher hardness values with water content, especially above 4%. This emphasizes that the hardness improvement observed for the FAC_15_4M formulation at high humidity is partly due to a reduction of the water content. This also explains the hardness improvement observed in the high humidity range for the FAC_5_12M and compared to the unstabilized formulation (**Fig. 8**.a) since the water content measured on the FAC_5_12M is always lower and does not exceed 4% (**Fig. 8**.b and **Fig. S1**.a). Regarding the evolution of hardness with water content, the FAC_5_12M formulation is even detrimental since the hardness values are always lower than the unstabilized samples for similar water contents.

For the Lev raw earth, the Lev_15_12M sample shows the highest hardness values in the whole humidity (**Fig. 8**.c) and water content (**Fig. 8**.d) ranges. The Lev_15_4M formulation shows very little variation of hardness in the whole humidity range (**Fig. 8**.c) and this is due to a nearly constant water content (**Fig. 8**.d). Even if the hardness at 98% RH is close to that of the Lev_15_12M sample, the water content is much lower (**Fig. 8**.d). For the Lev_15_4M formulation, the stabilization significantly reduces the adsorption and desorption of water. However, it should be noted that the hardness does not decrease at 98% RH despite a much higher water content. This could be explained by a higher degree of reaction of the slag favored by the higher water availability and by the longer equilibration time (42 days) needed at high humidity. As noted for the FAC raw earth, the LEV_5_12M formulation shows low water contents in the whole humidity range, and especially inferior to 4%, even at the highest humidity level (**Fig. 8**.c). The lower water contents for the Lev_5_12M than for the Lev_0_12M in the high humidity range explain the higher hardness values observed for RH superior to 65% (**Fig. 8**.b). Nevertheless, at the same water content, the Lev_5_12M formulation shows lower hardness values than the unstabilized one.

Regarding the SM samples, the highest hardness values are obtained for the SM_15_12M sample followed by the SM_5_12M sample and then the SM_15_4M sample either in terms of relative humidity (**Fig. 8**.e) or water content (**Fig. 8**.f). However, the hardness improvement with stabilization is much lower than for the other raw earth. The water content at high humidity is significantly reduced for all the formulations

(**Fig. 8**.f). For SM samples, the critical parameter for the stabilization seems to be the concentration of the activating solution over the content of added slag.

3.3 Porous Structure Characterization

For the three RE, the reduction in water content above 65% RH for the samples RE*_15_4M and RE*_5_12M as compared to unstabilized samples is associated to the reduction of capillary condensation in the macropores [60]. This results in an important reduction of capillary condensation for the three RE, characterized by a decrease in the total capillary pore volume (Eq. (7)) as illustrated in **Fig. 9**.a. and by the sorption isotherms performed on block samples, available as supplementary material (**Fig. S1**). The reduction in capillary volume also comes with a decrease in specific surface area (SSA) as compared to the RE*_0_12M formulations (**Fig. 9**.b). The decrease in SSA is explained by the flocculating effect of clayey particles and the closure of the interlayer clay sheets due to the interactions between the sodium of the activating solution and the negatively charged clay layers [58,61–63]. Increasing the slag content, while maintaining a similar sodium concentration, results in similar SSA for the RE*_15_4M formulations but to higher pore volume for the FAC and Lev formulations. The higher content of adsorbed water observed for the RE*_15_12M samples in the range of RH below 45% (**Fig. S1**) is associated to a higher proportion of fine pores in the structure and a higher specific surface area (**Fig. 9**.b). In fact, the RE*_15_12M formulations have similar or slightly higher specific surface area than the unstabilized samples but a lower pore volume. The evolution of the pore volume and SSA among the formulations is similar for the all three RE, although less pronounced for the SM formulations.

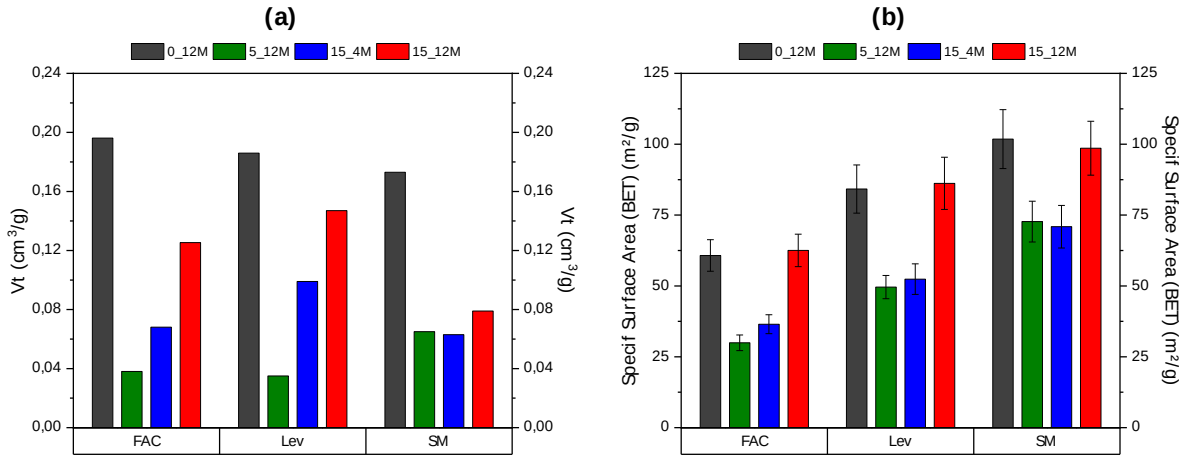

Fig. 9: Evolution of (a) the total capillary volume *Vt* and (b) the specific surface area (BET) for the formulations of the three RE.

4 Discussion

Suitability of instrumented indentation to characterize the properties of stabilized RE at a local scale

Spherical indentation enables the estimation of local mechanical properties of RE and stabilized RE, i.e. hardness and Young's modulus, parameters shown to be highly correlated in this work (**Fig. 4**). No macro-

crack is noted at the sample surface that could affect the measurement of *E* or *H*, thanks to the use of a spherical tip (**Fig. 2**) [26]. The typical contact diameter of the indented zone ranges from 900 to 1800 µm (**Fig. 2** and **Fig. 5**) which is more than 3 times the maximum particle size (400 µm for raw earth particles and 40 µm for slag grains). Especially, the influence of heterogeneities such as entrapped air defects (**Fig. 2**) is limited in instrumented indentation as compared to flexion testing where it can initiate a premature failure. Moreover, the relatively large volume tested allows to average the respective mechanical contributions of clays, slag and porosity present in the material, which is demonstrated by the limited relative scatter in the measurements (around 15%). This value is close to those already measured on other mineral materials: 10% on porous alumina (single phase with nano-sized pores) [44], 10% on hardened gypsum (single phase with micron sized pores) [64]. Here the material is rather heterogeneous at the scale of the indentation imprint scale: multiphase materials (slag and raw clay), presence of unhydrated grains and of large pores, which can explain the larger relative scatter. Instrumented indentation testing appears as a suitable technique for evaluating the effectiveness of slag stabilization in reinforcing raw soil, especially in wet conditions (**Fig. 7**.c). Indeed, one of the main advantages of this test method is the characterization of small samples, which allows the moisture equilibrium inside the specimen to be reached in a shorter time. Moreover, the use of small samples makes it possible to study samples of pure paste obtained from the finest fraction of the raw earth while limiting the cracking due to restrained shrinkage.

The hardness of unstabilized RE, and thus the cohesion of raw earth particles, decreases significantly as the relative humidity of the surrounding atmosphere increases, especially above 45% HR (**Fig. 7**.a). This decrease in hardness is due to the increase in water content on the sample by sorption and capillary condensation in the pores of the material and the subsequent decrease in bonds between clays due to the reduction in water suction [23,34] or in capillary forces [35]. In the case of unstabilized samples, the hardness decreases exponentially with water content (**Fig. 7** and **Table 4**). However, when RE is stabilized, the decrease in hardness with relative humidity and water content is strongly limited as compared to unstabilized samples (**Fig. 7**.c). This emphasizes the effectiveness of stabilization in limiting the water sensitivity of raw soils. Stabilization also reduces the differences in the measured mechanical properties among the three tested raw earth, thus limiting the influence of raw earth mineralogy on hardness.

Influence of the microstructure on hardness improvement

Two main mechanisms are identified for the improvement in hardness and reduction in moisture sensitivity with the stabilization of RE: the microstructural organization of clayey particles and the formation, through slag hydration, of a network of hydrates intertwined with the clayey matrix.
When the slag content (i.e. 5 wt%) or the NaOH content (i.e. 4 M) are too low to produce a network of hydrates that percolates through the material [36], the hardness improvement remains unsignificant under endogenous conditions (**Fig. 6**). The improvement in hardness with increasing relative humidity for these samples as compared to unstabilized RE*_0_12M samples (**Fig. 8**.a, c, e) is mainly due to a reduction in the water content (**Fig. 8**.b d, f) through the decrease in their sorption capacity. This decrease is characterized by a reduction of the capillary volume and of the SSA measured from the sorption isotherms (**Fig. 9**). In particular, the microstructures of stabilized samples are much denser than the unstabilized ones that present large capillary pores [36]. The addition of weakly activated slag grains tends to decrease the total pore volume of the material as the presence of sodium cations favors the flocculation of the clayey

particles, especially around the slag grains, leading to a decrease of the SSA. This explains why the water contents in the RE*_5_12M and RE*_15_4M samples remain relatively low (< 4%) even at high RH (**Fig. 8**.b, d, f). Since the decrease in hardness is well correlated with an increase in water content (up to 6%) for unstabilized samples (**Fig. 7**.b), the relative stability of hardness with relative humidity for RE*_5_12M and RE*_15_4M samples can be explained by a limited water content (typically below 4%).
The presence of a higher amount of slag between RE_5_12M and RE_15_4M limits the reorganization of clayey particles due to the interaction between sodium and the surface of the slag grains, which limits its adsorption by the clays, and to the spatial occupation of the slag grains, which are relatively large compared to the clays. The reader is
Finally, the relatively high hardness values measured at 98% RH for FAC_15_4M (11.5 MPa - **Fig. 8**.b) and Lev_15_4M (7.7 MPa - **Fig. 8**.d) samples may be due to the longer equilibration time (up to 45 days) at high RH needed to reach a constant mass which favors slag hydration and thus hydrates precipitation.

When the slag and sodium contents are sufficient to induce a satisfactory activation of the slag grains, typically in the RE*_15_12M samples, the microstructure formed is dense [36] with a similar SSA and a slightly lower capillary pore volume than the unstabilized samples (**Fig. 9**). This is explained by the precipitation of hydrates with a high SSA in the porosity of the material. Unlike the clayey particles, the electrostatic bonds between the hydrate particles are not significantly sensitive to water in the range of RH tested. Regarding FAC_15_12M and Lev_15_12M, a percolating network of C-A-S-H phases is formed, despite different structures [36]. In fact, the addition of 15 wt% of slag corresponds to a volume fraction of the binding phase equal to 19%, considering a CSH density around 2.0 g/cm^3 [65]. This is consistent with the values of the critical volume fraction required for percolation in multiphase materials with entangled structure found in the literature [66–68]. In these cases, despite relatively high water contents (> 4%), the hardness is improved in the whole RH range (**Fig. 8**.a - d). Especially, the hardness values of RE*_15_12M are almost twice as high as those of the unstabilized samples for similar water contents. In addition, the influence of the RE mineralogy is significantly reduced due to stabilization (**Fig. 7**.c). In the case of the SM_15_12M sample, the hardness improvement is lower than for the other RE*_15_12M samples, both under endogenous (**Fig. 6**.c) and controlled conditions (**Fig. 7**.c), especially at high water contents (**Fig. 8**.f). This is due to the precipitation of the outer product layer, which forms a shell on the surface of the slag grain [36]. This shell inhibits slag hydration and prevents the formation of a percolating network. This may explain why, in contrast to the others two RE, the hardness values present a plateau and no improvement with increasing slag content (**Fig. 6**.c). This illustrates the strong influence of the mineralogy of RE on their properties. For more detailed information on the microstructural organization of the samples, please refer to the companion article [36].

5 Conclusion

Spherical instrumented indentation appears to be a relevant technique to characterize the mechanical properties of the stabilized raw earths. The main advantages of this characterization method are: the limitation of cracking, the measurement at a local scale of the average properties of the different entangled phases (clay, sand or hydrate particles), the possibility of performing a statistically representative number of measurements on the same sample and the use of small samples which enables a faster moisture equilibration under different RH conditions. This enables to characterize pure binder samples, containing only the finest granulometric fraction of the RE.

The stabilization of three different raw earths by alkali-activated slag enabled to increase the hardness and the elastic modulus of the three different RE, especially in high RH conditions. However, the efficiency of the stabilization with respect to the water content depends on the mineralogy of the RE, and especially on its clayey activity by modifying the alkaline conditions of activation of the slag. The relative influence of the critical parameters of stabilization, i.e. slag content and concentration of the activating solution, depends on the mineralogical composition of the raw earth. In fact, the hardness improvement measured in the RH range is related to two different mechanisms: (i) the structural organization of the clayey particles, mainly influenced by the sodium content, which reduces the sorption capacity and therefore the amount of free water, and (ii) the formation of a percolating network of hydrates by slag hydration, which decreases the water sensitivity. Finally, the stabilization of raw earth shows an important influence on the pore volume and size distribution in the stabilized samples, but a limited effect on the microstructure of the clayey particles.

Acknowledgements
This work was funded by the French Ministry of Education and Research, through UdF PhD grant (allocation MSER – 2017).

Supplementary material

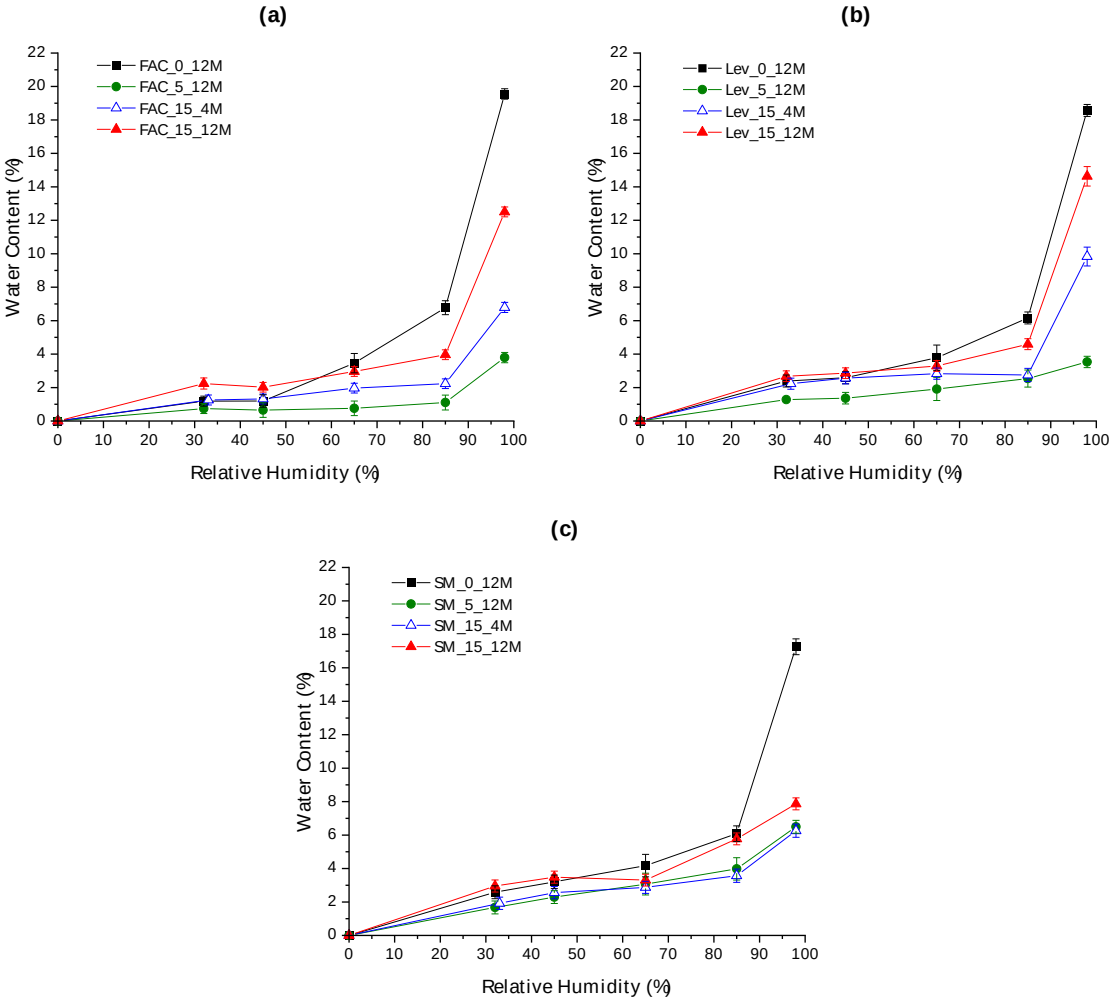

Fig. S1: Evolution of the water content with relative humidity for the (a) FAC, (b) Lev and (c) SM formulations. The sorption isotherms are performed on block samples equilibrated under the same environmental conditions as those on which the mechanical tests are performed

References

[1] F. McGregor, A. Heath, D. Maskell, A. Fabbri, J.-C. Morel, A review on the buffering capacity of earth building materials, Proc. Inst. Civ. Eng. - Constr. Mater. 169 (2016) 241–251. https://doi.org/10.1680/jcoma.15.00035.

[2] O.F. Osanyintola, C.J. Simonson, Moisture buffering capacity of hygroscopic building materials: Experimental facilities and energy impact, Energy Build. 38 (2006) 1270–1282. https://doi.org/10.1016/j.enbuild.2006.03.024.

[3] S. Liuzzi, M.R. Hall, P. Stefanizzi, S.P. Casey, Hygrothermal behaviour and relative humidity buffering of unfired and hydrated lime-stabilised clay composites in a Mediterranean climate, Build. Environ. 61 (2013) 82–92. https://doi.org/10.1016/j.buildenv.2012.12.006.

[4] A. Fabbri, J.C. Morel, Earthen materials and constructions, in: Nonconv. Vernac. Constr. Mater., Woodhead Publishing., Sawston, UK, 2016: pp. 273–299. https://doi.org/10.1016/B978-0-08-100038-0.00010-X.

[5] J.C. Morel, Q.B. Bui, E. Hamard, Weathering and durability of earthen material and structures, in: Mod. Earth Build. Mater. Eng. Constr. Appl., Woodhead Publishing, 2012: pp. 282–303. https://doi.org/10.1533/9780857096166.2.282.

[6] C.T.S. Beckett, P.A. Jaquin, J.-C. Morel, Weathering the storm: A framework to assess the resistance of earthen structures to water damage, Constr. Build. Mater. 242 (2020). https://doi.org/10.1016/j.conbuildmat.2020.118098.

[7] H. Van Damme, H. Houben, Earth concrete. Stabilization revisited, Cem. Concr. Res. 114 (2018) 90–102. https://doi.org/10.1016/j.cemconres.2017.02.035.

[8] M. Moevus, Y. Jorand, C. Olagnon, S. Maximilien, R. Anger, L. Fontaine, L. Arnaud, M.R. Moevus Á Anger, R. Anger, Y. Jorand, Á.C. Olagnon Á S Maximilien, C. Olagnon, S. Maximilien, L. Fontaine Ecole Nationale Supérieure, L. Arnaud, Earthen construction: an increase of the mechanical strength by optimizing the dispersion of the binder phase, Mater. Struct. 49 (2016) 1555–1568. https://doi.org/10.1617/s11527-015-0595-5.

[9] K. Scrivener, Calcined Clays for Sustainable Concrete, 2015. https://doi.org/10.1007/978-94-017-9939-3.

[10] H. Houben, H. Guillaud, Traité de Construction en Terre, CRATerre, Parenthèses, Marseille, 2006.

[11] A. Arrigoni, A.-C. Ecile Grillet, R. Pelosato, G. Dotelli, C.T.S. Beckett, M. Woloszyn, D. Ciancio, Reduction of rammed earth's hygroscopic performance under stabilisation: an experimental investigation, Build. Environ. 115 (2017) 358–367. https://doi.org/10.1016/j.buildenv.2017.01.034.

[12] A.W. Bruno, D. Gallipoli, C. Perlot, J. Mendes, Effect of stabilisation on mechanical properties, moisture buffering and water durability of hypercompacted earth, Constr. Build. Mater. 149 (2017) 733–740. https://doi.org/10.1016/j.conbuildmat.2017.05.182.

[13] M. Saidi, A. Soukaina Cherif, B. Zeghmati, E. Sediki, Stabilization effects on the thermal conductivity and sorption behavior of earth bricks, Constr. Build. Mater. 167 (2018) 566–577. https://doi.org/10.1016/j.conbuildmat.2018.02.063.

[14] F. Mcgregor, A. Heath, E. Fodde, A. Shea, Conditions affecting the moisture buffering measurement performed on compressed earth blocks, Build. Environ. 75 (2014) 11–18. https://doi.org/10.1016/j.buildenv.2014.01.009.

[15] C. Chen, G. Habert, Y. Bouzidi, A. Jullien, A. Ventura, LCA allocation procedure used as an incitative method for waste recycling: An application to mineral additions in concrete, Resour. Conserv. Recycl. 54 (2010) 1231–1240. https://doi.org/10.1016/j.resconrec.2010.04.001.

[16] G. Habert, J.B. D'Espinose De Lacaillerie, N. Roussel, An environmental evaluation of geopolymer based concrete production: Reviewing current research trends, J. Clean. Prod. (2011).

[17] U. De Filippis, E. Prud'homme, S. Meille, Sodium hydroxide substitution in slag activating mixes : A

potential pathway to more sustainable slag-based binders, Constr. Build. Mater. 300 (2021) 124183. https://doi.org/10.1016/j.conbuildmat.2021.124183.
[18] A. Wilkinson, A. Haque, J. Kodikara, Stabilisation of clayey soils with industrial by-products: part A, in: Proc. Inst. Civ. Eng., ICE Publishing, 2010: pp. 149–163. https://doi.org/10.1680/grim.2010.163.3.149.
[19] A. Wilkinson, A. Haque, J. Kodikara, Stabilisation of clayey soils with industrial by-products: Part B, Proc. Inst. Civ. Eng. Gr. Improv. 163 (2010) 165–172. https://doi.org/10.1680/grim.2010.163.3.165.
[20] P. Sargent, P.N. Hughes, M. Rouainia, M.L. White, The use of alkali activated waste binders in enhancing the mechanical properties and durability of soft alluvial soils, Eng. Geol. 152 (2013) 96–108. https://doi.org/10.1016/j.enggeo.2012.10.013.
[21] P. Sargent, The development of alkali-activated mixtures for soil stabilisation, in: F. Pacheco-Torgal, J.A. Labrincha, C. Leonelli, A. Palomo, P. Chindaprasirt (Eds.), Handb. Alkali-Activated Cem. Mortars Concr., Woodhead Publishing Limited, 2015: pp. 555–604.
[22] G.N. Obuzor, J.M. Kinuthia, R.B. Robinson, Soil stabilisation with lime-activated-GGBS-A mitigation to flooding effects on road structural layers/embankments constructed on floodplains, Eng. Geol. 151 (2012) 112–119. https://doi.org/10.1016/j.enggeo.2012.09.010.
[23] C.T.S. Beckett, C.E. Augarde, D. Easton, T. Easton, Strength characterisation of soil-based construction materials, Géotechnique. 68 (2018) 400–409. https://doi.org/10.1680/jgeot.16.P.288.
[24] S. Horpibulsuk, R. Rachan, A. Chinkulkijniwat, Y. Raksachon, A. Suddeepong, Analysis of strength development in cement-stabilized silty clay from microstructural considerations, Constr. Build. Mater. 24 (2010) 2011–2021. https://doi.org/10.1016/j.conbuildmat.2010.03.011.
[25] L. Xu, K.K. Wong, A. Fabbri, F. Champiré, D. Branque, Loading-unloading shear behavior of rammed earth upon varying clay content and relative humidity conditions, Soils Found. 58 (2018) 1001–1015. https://doi.org/10.1016/j.sandf.2018.05.005.
[26] S. Meille, M. Gallo, P. Clément, S. Tadier, J. Chevalier, Spherical instrumented indentation as a tool to characterize porous bioceramics and their resorption, J. Eur. Ceram. Soc. 39 (2019) 4459–4472. https://doi.org/10.1016/j.jeurceramsoc.2019.06.040.
[27] W.C.C. Oliver, G.M.M. Pharr, An improved technique for determining hardness and elastic modulus using load and displacement sensing indentation experiments, J. Mater. Res. 7 (1992) 1564–1583. https://doi.org/10.1557/jmr.1992.1564.
[28] W.C. Oliver, G.M. Pharr, Measurement of hardness and elastic modulus by instrumented indentation: Advances in understanding and refinements to methodology, J. Mater. Res. 19 (2004) 3–20. https://doi.org/10.1557/jmr.2004.19.1.3.
[29] R. Song, Y. Wang, S. Sun, M. Cui, J. Liu, Evaluation of elastoplastic properties of brittle sandstone at microscale using micro-indentation test and simulation, Energy Sci. Eng. 8 (2020) 3490–3501. https://doi.org/10.1002/ese3.759.
[30] F.P. Ganneau, G. Constantinides, F.J. Ulm, Dual-indentation technique for the assessment of strength properties of cohesive-frictional materials, Int. J. Solids Struct. 43 (2006) 1727–1745. https://doi.org/10.1016/j.ijsolstr.2005.03.035.
[31] W. Li, M. Wang, J. Cheng, Indentation hardness of the cohesive-frictional materials, Int. J. Mech. Sci. 180 (2020) 105666. https://doi.org/10.1016/j.ijmecsci.2020.105666.
[32] P. Clément, S. Meille, J. Chevalier, C. Olagnon, Mechanical characterization of highly porous inorganic solids materials by instrumented micro-indentation, Acta Mater. 61 (2013) 6649–6660. https://doi.org/10.1016/j.actamat.2013.07.005.
[33] F. Champiré, A. Fabbri, J.-C.C. Morel, H. Wong, F. McGregor, Impact of relative humidity on the mechanical behavior of compacted earth as a building material, Constr. Build. Mater. 110 (2016) 70–78. https://doi.org/10.1016/j.conbuildmat.2016.01.027.
[34] P.A. Jaquin, C.E. Augarde, D. Gallipoli, D.G. Toll, The strength of unstabilised rammed earth

materials, Géotechnique. 59 (2009) 487–490. https://doi.org/10.1680/geot.2007.00129.
[35] H. Van Damme, M. Zabat, J.-P. Laurent, P. Dudoignon, A. Pantet, D. Gélard, H. Houben, Nature and Distribution of Cohesion Forces in Earthen Building Materials, in: N. Agnew (Ed.), Conserv. Anc. Sites Silk Road, Getty Publ, 2010: pp. 181–188.
[36] U. De Filippis, E. Prud'homme, S. Meille, Impact of the interaction between clay particles and alkali solution in the context of slag-stabilized poured raw earth, Submitted. (2023).
[37] G. Alves de Azeredo, Mise au point de procédures d'essais mécaniques sur mortiers de terre, application à l'étude de leur rhéologie, Institut National des Sciences Appliqués de Lyon, 2005.
[38] H. Van Damme, M. Ben Ohoud, From flow to fracture and fragmentation in colloidal media, Disord. Fract. (1990) 105–116.
[39] L. Caner, Phyllosilicates des sols : de l'identification à la quantification, 2011.
[40] I. Aksu, E. Bazilevskaya, Z. Karpyn, W. Leone, Swelling of clay minerals in unconsolidated porous media and its impact on permeability, GeoResJ. 7 (2015) 1–13. https://doi.org/10.1016/j.grj.2015.02.003.
[41] A.W.W. Skempton, The Colloidal "Activity" of Clays, in: Sel. Pap. Soil Mech., Thomas Telford Limited, London, 1984: pp. 60–64. https://doi.org/10.1680/sposm.02050.0009.
[42] U. De Filippis, E. Prud'homme, S. Meille, Relation between Activator Ratio, Hydration Products and Mechanical Properties of Alkali-activated Slag, Constr. Build. Mater. 266 (2021). https://doi.org/10.1016/j.conbuildmat.2020.120940.
[43] P. CLEMENT, Détermination des Propriétés Mécaniques de Céramiques Poreuses par Essais de Microindentation Instrumentée Sphérique, INSA de Lyon, 2013.
[44] D. Staub, S. Meille, V. Le Corre, L. Rouleau, J. Chevalier, Identification of a damage criterion of a highly porous alumina ceramic, Acta Mater. 107 (2016) 261–272. https://doi.org/10.1016/j.actamat.2016.01.071.
[45] M. Moula, Résistance mécanique des alumines mésoporeuses, influence de la morphologie microstructurale, INSA de Lyon, 2020.
[46] M. Moula, S. Meille, V. Le Corre, J. Chevalier, Mechanical characterization of meso-porous alumina by micro-and nano-indentation, Mater. Today Commun. 25 (2020). https://doi.org/10.1016/j.mtcomm.2020.101315.
[47] M. Miller, C. Bobko, M. Vandamme, F.J. Ulm, Surface roughness criteria for cement paste nanoindentation, Cem. Concr. Res. 38 (2008) 467–476. https://doi.org/10.1016/j.cemconres.2007.11.014.
[48] P. Maiti, M. Bhattacharya, P.S. Das, P.S. Devi, A.K. Mukhopadhyay, Indentation size effect and energy balance issues in nanomechanical behavior of ZTA ceramics, Ceram. Int. 44 (2018) 9753–9772. https://doi.org/10.1016/j.ceramint.2018.02.210.
[49] Y. Bala, B. Depalle, D. Farlay, T. Douillard, S. Meille, H. Follet, R. Chapurlat, J. Chevalier, G. Boivin, Bone micromechanical properties are compromised during long-term alendronate therapy independently of mineralization, J. Bone Miner. Res. 27 (2012) 825–834. https://doi.org/10.1002/jbmr.1501.
[50] B.R. Lawn, Indentation of Ceramics with Spheres: A Century after Hertz, J. Am. Ceram. Soc. 81 (1998) 1977–94.
[51] S. Pathak, S.R. Kalidindi, Spherical nanoindentation stress–strain curves, Mater. Sci. Eng. R Reports. 91 (2015) 1–36. https://doi.org/10.1016/J.MSER.2015.02.001.
[52] L.H. He, N. Fujisawa, M. V. Swain, Elastic modulus and stress-strain response of human enamel by nano-indentation, Biomaterials. 27 (2006) 4388–4398. https://doi.org/10.1016/j.biomaterials.2006.03.045.
[53] S. Brunauer, P.H. Emmett, E. Teller, Adsorption of Gases in Multimolecular Layers, J. Am. Chem. Soc. 60 (1938) 309–319.

[54] M. Babaee, A. Castel, Water vapor sorption isotherms, pore structure, and moisture transport characteristics of alkali-activated and Portland cement-based binders, Cem. Concr. Res. 113 (2018) 99–120. https://doi.org/10.1016/j.cemconres.2018.07.006.
[55] J. Rouquerol, D. Avnir, F. C.W, D.. Everett, J.. Haynes, N. Pernicone, J.D.. Ramsay, K.S.. Sing, K.. Unger, Recommendations for the characterization of porous solids, Pure Appl. Chem. 66 (1994) 1739–1758.
[56] M. Naderi, Surface Area: Brunauer-Emmett-Teller (BET), in: S. Tarleton (Ed.), Prog. Filtr. Sep., Academic Press, 2015: pp. 585–608. https://doi.org/10.1016/B978-0-12-384746-1.00014-8.
[57] U. De Filippis, E. Prud'homme, S. Meille, Terre coulée stabilisée par activation alcaline : Etude des phénomènes physico-chimiques et de leurs impacts sur les propriétés d'usage, in: NoMaD, Actes Du Colloq., Liège, Belgique, 2018.
[58] J. Stawinski, J. Wierzchos, M.T. Garcia-Gonzalez, Influence of Calcium and Sodium Concentration on the Microstructure of Bentonite and Kaolin, Clays Clay Miner. 38 (1990) 617–622. https://doi.org/10.1346/CCMN.1990.0380607.
[59] A. Marsh, A. Heath, P. Patureau, P. Evernden, P. Walker, Influence of clay minerals and associated minerals in alkali activation of soils, Constr. Build. Mater. 229 (2019). https://doi.org/10.1016/j.conbuildmat.2019.116816.
[60] M. Hall, D. Allinson, Analysis of the hygrothermal functional properties of stabilised rammed earth materials, Build. Environ. 44 (2009) 1935–1942. https://doi.org/10.1016/j.buildenv.2009.01.007.
[61] M.S. Zbik, R. StC Smart, G.E. Morris, Kaolinite flocculation structure, J. Colloid Interface Sci. 328 (2008) 73–80. https://doi.org/10.1016/j.jcis.2008.08.063.
[62] E. Tombácz, M. Szekeres, Surface charge heterogeneity of kaolinite in aqueous suspension in comparison with montmorillonite, Appl. Clay Sci. 34 (2006) 105–124. https://doi.org/10.1016/j.clay.2006.05.009.
[63] N. Wilkinson, A. Metaxas, C. Quinney, S. Wickramaratne, T.M. Reineke, C.S. Dutcher, pH dependence of bentonite aggregate size and morphology on polymer-clay flocculation, Colloids Surfaces A. 537 (2018) 281–286. https://doi.org/10.1016/j.colsurfa.2017.10.007.
[64] P. Clément, S. Meille, J. Chevalier, C. Olagnon, Mechanical characterization of highly porous inorganic solids materials by instrumented micro-indentation, Acta Mater. 61 (2013). https://doi.org/10.1016/j.actamat.2013.07.005.
[65] S. Bahafid, S. Ghabezloo, M. Duc, P. Faure, J. Sulem, Effect of the hydration temperature on the microstructure of Class G cement: C-S-H composition and density, Cem. Concr. Res. 95 (2017) 270–281. https://doi.org/10.1016/j.cemconres.2017.02.008.
[66] E.J. Garboczi, Percolation phase diagrams for multi-phase models built on the overlapping sphere model, Phys. A Stat. Mech. Its Appl. 442 (2016) 156–168. https://doi.org/10.1016/j.physa.2015.09.014.
[67] D.P. Bentz, E.J. Garboczi, Percolation of phases in a three-dimensional cement paste microstructural model, Cem. Concr. Res. 21 (1991) 325–344. https://doi.org/10.1016/0008-8846(91)90014-9.
[68] H. Scher, R. Zallen, Critical Density in Percolation Processes, J. Chem. Phys. 53 (1970) 3759.